C. R. Mecanique 345 (2017) 807–823

Contents lists available at ScienceDirect

Comptes Rendus Mecanique

www.sciencedirect.com

# Effects of modal truncation and condensation methods on the Frequency Response Function of a stage reducer connected by rigid coupling to a planetary gear system

Marwa Bouslema [a,b,*], Ahmed Frikha [a], Moez Abdennadhar [a], Tahar Fakhfakh [a], Rachid Nasri [b], Mohamed Haddar [a]

[a] Mechanical Modeling and Manufacturing Laboratory (LA2MP), National School of Engineers of Sfax, University of Sfax, BP 1173-3038, Sfax, Tunisia

[b] Applied Mechanics and Engineering, University of El-Manar II, 1002 Tunis, Tunisia

ARTICLE INFO

*Article history:*
Received 16 June 2017
Accepted 26 September 2017
Available online 2 November 2017

*Keywords:*
Coupling method
Planetary transmission
Frequency Response Function
Frequency based substructuring
Condensation
Modal truncation

ABSTRACT

The present paper is aimed at the application of a substructure methodology, based on the Frequency Response Function (FRF) simulation technique, to analyze the vibration of a stage reducer connected by a rigid coupling to a planetary gear system. The computation of the vibration response was achieved using the FRF-based substructuring method. First of all, the two subsystems were analyzed separately and their FRF were obtained. Then the coupled model was analyzed indirectly using the substructuring technique. A comparison between the full system response and the coupled model response using the FRF substructuring was investigated to validate the coupling method. Furthermore, a parametric study of the effect of the shaft coupling stiffness on the FRF was discussed and the effects of modal truncation and condensation methods on the FRF of subsystems were analyzed.



## 1. Introduction

Transmission systems are widely used in manufacturing applications due to their power advantages, decreased cost, and high efficiency. The multi-stage gears generally have larger reduction ratios and greater load transmissions. Dynamic models of transmission systems, including parallel and planetary gears, were widely investigated in literature [1–3]. Several issues have made the parallel gear specially interesting. The effects of bearing flexibilities and axial vibrations of a parallel gear were studied in [4,5]. Planetary gears are used in transmission applications such as wind turbines and helicopters, requiring a higher transmission torque. A great deal of research focused on the static and dynamic models of a planetary transmission system, created by adopting the lumped mass method [6] and the finite element (FE) model [7]. The dynamic behavior of a planetary transmission system was investigated in [8,9]. The sensitivity of natural frequencies and vibration modes in compound planetary gears were analyzed in [10]. On the other hand, a lot of research investigated the dynamic behavior of a gearbox model formed by two transmission systems which are the planetary and the parallel gears [11–14]. Such

* Corresponding author at: Mechanical Modeling and Manufacturing Laboratory (LA2MP), National School of Engineers of Sfax, University of Sfax, BP 1173-3038, Sfax, Tunisia.
*E-mail address:* marwa.bouslema@yahoo.fr (M. Bouslema).

https://doi.org/10.1016/j.crme.2017.09.008
1631-0721/

transmission systems are widely used in wind turbine gearboxes (WTG). Peeters et al. [15] developed the flexible multibody dynamics model of a wind turbine transmission system in multibody dynamics software and studied its natural frequencies and vibration modes. Feng and Zuo [16] investigated the vibration signal models for planetary gearbox fault diagnosis.

The dynamic analysis of complex transmission systems requires much more Central Processing Unit (CPU) and computation time. In order to simplify this analysis and save their computational time, some researchers were interested in the study of the substructuring method and component mode synthesis [17,18]. These methods are used to build the dynamic response of complex systems by assembling the dynamic models from its subsystems. These subsystems can be expressed by spatial mass, stiffness, damping data, modal data, or receptances (dynamic compliance). The major concept of the substructuring method is to use the Frequency Response Function (FRF) for computing the vibration response of the free subsystem. The overall coupled system response is then composed by the dynamic compliance theory [19] thanks to the dynamic stiffness terms at the coupling coordinates of the subsystems [20]. This kind of coupling can be either rigid or flexible with the dynamic stiffness [21]. Some techniques of substructuring, as coupling and decoupling methods were proposed in [22–24]. Nevertheless, the coupling method applied to gears systems is quite limited in the literature. Unlike coupling, the decoupling method was developed for the transmission system in [23,25]. In the literature, the coupling method was investigated for coupling two subsystems in other applications such as automotive ones in [21,26] and rotating systems in [22] based on the FRF. In this context, the analytic receptance coupling method was developed by Bishop and Johnson [18]. The greatest advantage of this approach is its ability to increase efficiency and decrease the computation time. Furthermore, the use of FRF provides a common basis to combine subsystems of numerical and experimental origins.

The condensation method and the modal truncation are used in the analysis of complex systems to reduce the computation time and the problem size. Different reduction modes approaches were proposed in the literature to construct the reduction basis of a subsystem such as the condensation and the truncated modes. The dynamic condensation was applied to investigate the influences of neighboring subsystems and coupling on the FRF of each subsystem in [25,27]. The modal truncation problem faced with in the responses of some applications was treated in [26,28–31], and the effect of truncation modes was analyzed in [28]. A modal based approach for decoupling associated with modal truncation was presented in [30]. In addition, Ambrogio and Fregolent [30] studied the effect of modal truncation on the natural frequencies by decreasing the number of modes. Suarez [32] introduced a force derivative method to analyze the effect of the truncated higher modes in the representation of the response of the substructures. Only the modes located in the interesting frequency range were considered in the dynamic analysis. In fact, modal truncation was used to express the contribution of the out-of-range modes on the FRFs of each subsystem.

In this paper, the application of the substructuring technique was investigated for the analysis of the vibration signals of a transmission system, consisting of two gear stages, which are the parallel and planetary gear systems. The present method was developed in order to reduce the size of the computational problem and the complexity of the dynamic model. In fact, the analysis of the global system is more difficult than that of the local dynamic behavior. If one subsystem is replaced by another with a known FRF, this method becomes useful and allows a rapid computation of the FRF of the whole system. In addition, the substructuring method is interested in some applications of damage detection in gear systems [16]. The modal truncation was investigated to obtain a consistent basis for truncation modes of substructures in the vibratory analysis of a complex system.

The remaining of this paper is organized as follows. The dynamic models of planetary gear and parallel stage are described in section 2. The theoretical principles of the substructuring method are treated in section 3. The results of the FRF coupling method were compared to those of the FRF of the full system in section 4. The effects of condensation and modal truncation were investigated in section 5 before drawing the major conclusions in the final section.

## 2. Motion equation

The studied transmission system consists of two subsystems: a first subsystem $A$ connected to a second subsystem $B$ by a rigid coupling, corresponding respectively to a parallel and to a planetary gear stage. The models of the parallel stage and the spur planetary gears were established by adopting the lumped parameter model (Fig. 1). The parallel stage gear is similar to the model proposed by Kahraman [5]. Nevertheless, eight DoFs were used to describe the gear system behavior rather the ten DoFs adopted by [5]. The displacements of the radial gears were not taken into account in the reference model. Both gears are seated on two rigid shafts, supported by flexible bearings.

The gears are modeled by rigid disks of masses $m_1$ and $m_2$, polar mass moments of inertia about $z$-axis $J_1$ and $J_2$ and diametral mass moments of inertia about the $y$-axis $I_1$ and $I_2$. The second gear is connected to the planetary gear. The gear-mesh is represented by linear springs along the action line. The gear mesh stiffness is assumed constant. The radial and the axial stiffness bearings are denoted by $k_{yj}$ and $k_{zj}$ respectively. The second shaft of the reducer is connected to the sun shaft by a rigid coupling of inertia $I_A$. The shafts are supported by bearings, modeled by linear springs. The gears are modeled by concentrated masses. The planetary gear train components such as ring, carrier, sun, and $N$ planets are assumed to be rigid bodies. Each one of these components of the planetary train has three degrees of freedom: two translations and one rotation. The rotation coordinates are denoted by $w_j = r_j\theta_j$ $(j = c, r, s)$, where $\theta_j$ is the rotation angle, $r_j$ is the base circle radius of the sun. In Fig. 2, $u_i$, $v_i$, and $w_i$ $(i = c, s, r)$ are respectively the displacements of the sun gear, the carrier and the ring in two radials and rotational directions. The planetary gear system was investigated in [33]. $k_{cu}$ and $k_{su}$ are the support stiffness of the carrier and the sun gears in the $u$ direction, respectively. $k_{cv}$ and $k_{sv}$ are the support stiffness

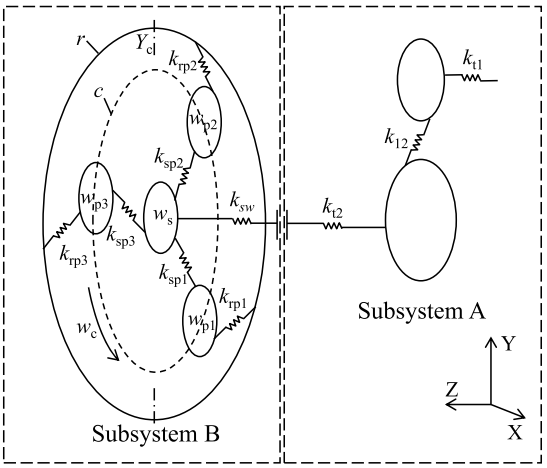


**Fig. 1.** A stage reducer connected by a rigid coupling to a planetary gear system.

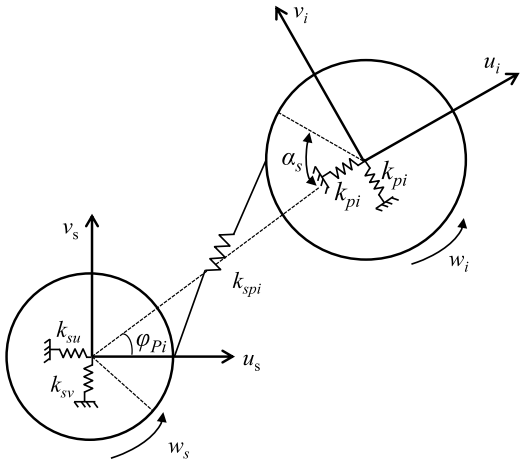


**Fig. 2.** Sun planet gear mesh modeling.

of the carrier and sun gears in $v$ direction, respectively. $k_{sw}$ and $k_{cw}$ are the torsional stiffness of the carrier and sun gears. $\alpha_s$ is the pressure angle of the sun/planet mesh shown in Fig. 2. Circumferential planet emplacement are determined by the angle $\varphi_p$, where $\varphi_p$ is connected to the rotating vector $i$ with $\varphi_1 = 0$. The displacements $\delta_{sp}$ and $\delta_{rp}$ along the lines of action are formulated by [33]:

$$\begin{aligned}\delta_{sp} &= v_s \cos\varphi_{sp} - u_s \sin\varphi_{sp} - u_p \sin\alpha_s - v_p \cos\alpha_s + w_s + w_p \\ \delta_{rp} &= v_r \cos\varphi_{rp} - u_c \sin\varphi_{rp} + u_p \sin\alpha_r - v_p \cos\alpha_r + w_r - w_p\end{aligned} \tag{1}$$

where $\varphi_{sp} = \varphi_p - \alpha_s$, $\varphi_{rp} = \varphi_p - \alpha_r$, $\alpha_s$ and $\alpha_r$ are the pressure angles of ring and sun gears.

The damping is neglected when the analyses are bounded to frequency calculations. Furthermore, both the planet carrier and the parallel output shaft are free at their boundaries. Using the Lagrange formulation allows finding the degree of freedom of the system. The motion equation is expressed by:

$$[\boldsymbol{M}]\left\{\ddot{\boldsymbol{U}}(t)\right\} + [\boldsymbol{C}]\left\{\dot{\boldsymbol{U}}(t)\right\} + [\boldsymbol{K}]\{\boldsymbol{U}(t)\} = \{\boldsymbol{F}(t)\} \tag{2}$$

where $[\boldsymbol{K}]$, $[\boldsymbol{M}]$ and $[\boldsymbol{C}]$ are the stiffness, mass, and damping matrices, respectively. $\{\boldsymbol{F}(t)\}$ and $\{\boldsymbol{U}(t)\}$ are the excitation forces and the displacement vectors, respectively. $t$ represents the time variable.

### 2.1. Substructure coupled method FRF

The substructure coupled method consists in dividing the global system $AB$ into two subsystems $A$ and $B$ as presented in Fig. 1. The first subsystem is made up of the stage reducer, which is a parallel gear stage. A modeling of planetary gear transmission was proposed in [33]. The two subsystems are coupled with a rigid coupling. The coupling is divided into two equal parts as in [34]. This coupling is inspired from the technique illustrated in [35]. Both subsystems $A$ and $B$ are modeled

by a linear spring and discrete masses corresponding to the mass–spring system. The gear mesh stiffness $[\boldsymbol{K}(t)]$ is modeled by a linear spring on the line of action of the meshing teeth. Eq. (2) is used to determine the mass $[\boldsymbol{M}]$ and the stiffness $[\boldsymbol{K}]$ of each subsystem. The stiffness matrix $[\boldsymbol{K}_i]$, where $i = A, B$, is expressed as:

$$[\boldsymbol{K}_i] = [\boldsymbol{K}_{bi}] + [\boldsymbol{K}(t)] \tag{3}$$

where $[\boldsymbol{K}_{bi}]$ presents the stiffness matrix of the bearings for each subsystem. $[\boldsymbol{K}(t)]$ is the time varying stiffness matrix, which is decomposed into an average stiffness matrix $[\boldsymbol{k}_m]$ and a time varying stiffness matrix $[\boldsymbol{k}(t)]$. In this paper, the gear stiffness is assumed constant and the time variable stiffness is neglected. The generalized coordinates vector of the subsystem $A$ includes 9 DoFs defined by:

$$\begin{aligned} &\boldsymbol{U_A} = [{}_A[\boldsymbol{U}]_i \ {}_A[U]_c]^{\mathrm{T}}, \qquad {}_A[\boldsymbol{U}]_i = \left[\, r_1\theta(1) \quad r_2\theta(2) \quad y_1 \quad y_2 \quad z_1 \quad z_2 \quad r_1\rho(y1) \quad r_2\rho(y2) \,\right]^{\mathrm{T}} \\ &{}_A[U]_c = [\theta(2,2)]^{\mathrm{T}} \end{aligned} \tag{4}$$

The generalized coordinates vector of the subsystem $B$ includes 22 DoFs and can be defined by:

$$\begin{aligned} &\boldsymbol{U_B} = \left[{}_B[U]_c \, , {}_B[\boldsymbol{U}]_j\right]^{\mathrm{T}}, \qquad {}_B[U]_c = [\theta(2,2)]^{\mathrm{T}} \\ &{}_B[\boldsymbol{U}]_j = \left[\, u_s \quad v_s \quad w_s \quad u_c \quad v_c \quad w_c \quad u_r \quad v_r \quad w_r \quad u_p1 \quad v_p1 \quad w_p1 \quad u_{pN} \quad v_{pN} \quad w_{pN} \,\right]^{\mathrm{T}} \end{aligned} \tag{5}$$

The DoFs of the subsystem can be partitioned into internal and coupling DoFs ${}_A[\boldsymbol{U}]_i$, ${}_B[\boldsymbol{U}]_j$, ${}_A[U]_c$ and ${}_B[U]_c$, respectively. The mass matrix $[\boldsymbol{M}_A]$ of subsystem $A$ is expressed by:

$$[\boldsymbol{M}_A] = \mathrm{diag}(J_1/r_1^2,\, J_2/r_2^2, m_1, m_2, m_1, m_2, I_1/r_1^2,\, I_2/r_2^2,\, I_A/2) \tag{6}$$

where $m_1$ and $m_2$ are the wheel and pinion mass. $I_1$, $I_2$ and $I_A$ are the wheel inertia, the pinion inertia and the coupling inertia, respectively. The rigidity matrix $[\boldsymbol{K}_{bA}]$ of subsystem $A$ is expressed by:

$$[\boldsymbol{K}_{bA}] = \mathrm{diag}(0, 0, k_{by1}, k_{by2}, k_{bz1}, k_{bz2}, k_{b\rho y1}, k_{b\rho y2}) \tag{7}$$

The average stiffness matrix $[\boldsymbol{k}_{\mathrm{m}}]$ is written as [5]:

$$[\boldsymbol{k}_{\mathrm{m}}] = k_{\mathrm{moy}}[\boldsymbol{q}][\boldsymbol{q}]^{\mathrm{T}} \tag{8}$$

where the vector $[\boldsymbol{q}]$ is given by:

$$[\boldsymbol{q}]^{\mathrm{T}} = \left[\, \cos\beta \quad -\cos\beta \quad \cos\beta \quad -\cos\beta \quad \sin\beta \quad -\sin\beta \,\right]^{\mathrm{T}} \tag{9}$$

where $\beta = 0$ is the helix angle.

The mass matrix $[\boldsymbol{M}_B]$ of the subsystem $B$ is expressed by:

$$[\boldsymbol{M}_B] = \mathrm{diag}\,(I_A/2, \quad M_s, \quad M_c, \quad M_r, \quad M_j, \quad \ldots, \quad M_N) \tag{10}$$

with $[\boldsymbol{M}_J] = \mathrm{diag}\,(m_j, \ m_j, \ I_j/(r_j)^2\,)$, $j = c, r, s, 1, \ldots, N$. $I_j$ is the inertia moment for the $j$th element.

The stiffness matrix of subsystem $B$, denoted by $[\boldsymbol{K}_B]$, is expressed in Appendix A.

### 2.2. Full system FRF

The direct method consists in analyzing the full system without its splitting into subsystems. This method is used as a reference for the validation of the substructuring method. The complete system, presented in Fig. 1, consists of a planetary gear and a stage reducer. The behavior of the dynamics of the full system is determined in terms of Frequency Response Functions (FRFs). The motion equations of the subsystem are considered in the time domain. The subsystem FRF can be determined theoretically. Taking into account the Lagrange formalism, the differential motion equation of the full system can be expressed by Eq. (2) by replacing $[\boldsymbol{M}]$, $[\boldsymbol{C}]$ and $[\boldsymbol{K}]$ by $[\boldsymbol{M}_{AB}]$, $[\boldsymbol{C}_{AB}]$ and $[\boldsymbol{K}_{AB}]$ respectively. The DoFs vector $[\boldsymbol{U}_{AB}]$ of the full system is expressed by:

$$[\boldsymbol{U}_{AB}] = \begin{bmatrix} r_1\theta(1) & r_2\theta(2) & y_1 & y_2 & z_1 & z_2 & r_1\rho(y1) & r_2\rho(y2) & \theta(2,2) & u_s & v_s & w_s & u_c & v_c & w_c & u_r \\ v_r & w_r & u_p1 & v_p1 & w_p1 & \ldots & u_pN & v_pN & w_pN & & & & & & & \end{bmatrix} \tag{11}$$

The mass matrix $[\boldsymbol{M}_{AB}]$ is expressed as:

$$[\boldsymbol{M}_{AB}] = \mathrm{diag}\left(J_1/r_1^2,\ J_2/r_2^2,\ m_1,\ m_2,\ m_1,\ m_2,\ I_1/r_1^2,\ I_2/r_2^2,\ I_A,\ M_s,\ M_c,\ M_r,\ M_{p1},\ \ldots,\ M_{pN}\right) \tag{12}$$

where $m_1$ and $m_2$ are the pinion and wheel mass. $I_1$, $I_2$ and $I(A)$ are the inertia of the wheel, the, pinion and the coupling, respectively.

## 3. Theoretical formulation

The frequency response Function-Based Substructuring (FBS) is applied to the dynamic behavior of a rigidly coupled system. This method is based on the free interface Frequency Response Functions (FRFs) of the uncoupled subsystems. The essential concept of FBS is to combine the FRF of each subsystem to collect the FRF of the full system. In the assembly procedure, the FRF represents the structural dynamic stiffness of the subsystems in the frequency domain, which can be determined theoretically or experimentally [36].

In this section, the methodology of the coupling technique was described. Two steps were used in this technique, which are the determination of the FRF of each subsystem and of their coupling. The procedure of an analytical FBS coupling consists in the determination of the FRF of the coupling system.

### 3.1. Coupling Frequency Response Functions (FRFs)

The FBS technique predicts the dynamic behavior of a coupled system on the basis of free-interface FRFs of the uncoupled subsystems and a possible coupling stiffness. For every subsystem, the available degrees of freedom (DoFs) are classified into two sets, namely (1) for the coupling DoFs and (2) for the internal DoFs. These internal DoFs correspond to the excitation and response DoFs. The receptance matrices of subsystems $A$ and $B$ in the frequency domain are expressed as in [17]:

$$\begin{bmatrix} {}_A[\boldsymbol{U}]_i \\ {}_A[\boldsymbol{U}]_c \end{bmatrix} = \begin{bmatrix} {}_A[\boldsymbol{H}]_{ii} & {}_A[\boldsymbol{H}]_{ic} \\ {}_A[\boldsymbol{H}]_{ci} & {}_A[\boldsymbol{H}]_{cc} \end{bmatrix} \begin{bmatrix} {}_A[\boldsymbol{F}]_i \\ {}_A[\boldsymbol{F}]_c \end{bmatrix}, \qquad \begin{bmatrix} {}_B[\boldsymbol{U}]_j \\ {}_B[\boldsymbol{U}]_c \end{bmatrix} = \begin{bmatrix} {}_B[\boldsymbol{H}]_{jj} & {}_B[\boldsymbol{H}]_{jc} \\ {}_B[\boldsymbol{H}]_{cj} & {}_B[\boldsymbol{H}]_{cc} \end{bmatrix} \begin{bmatrix} {}_B[\boldsymbol{F}]_j \\ {}_B[\boldsymbol{F}]_c \end{bmatrix} \tag{13}$$

where ${}_A[\boldsymbol{U}]_i$ and ${}_A[\boldsymbol{U}]_c$ (resp. ${}_B[\boldsymbol{U}]_j$ and ${}_B[\boldsymbol{U}]_c$) are the displacement vectors of a subsystem $A$ (resp. $B$). ${}_A[\boldsymbol{H}]_{ii}$, ${}_A[\boldsymbol{H}]_{ic}$, ${}_A[\boldsymbol{H}]_{ci}$ and ${}_A[\boldsymbol{H}]_{cc}$ (resp. ${}_B[\boldsymbol{H}]_{jj}$, ${}_B[\boldsymbol{H}]_{jc}$, ${}_B[\boldsymbol{H}]_{cj}$ and ${}_B[\boldsymbol{H}]_{cc}$) denote the FRFs matrices of subsystem $A$ (resp. $B$). ${}_A[\boldsymbol{F}]_i$ and ${}_A[\boldsymbol{F}]_c$ (resp. ${}_B[\boldsymbol{F}]_j$ and ${}_B[\boldsymbol{F}]_c$) are the force vectors of the subsystems $A$ (resp. $B$). Indices $i$, $j$ and $c$ refer to the subsystems $A$, $B$ and the coupled DoFs, respectively. The subsystem $A$ is rigidly connected to subsystem $B$ at DoFs $c$. Using Eq. (13), the combined system becomes:

$${}_{AB}[\boldsymbol{U}] = {}_{AB}[\boldsymbol{H}]\,{}_{AB}[\boldsymbol{F}], \qquad {}_{AB}[\boldsymbol{U}] = \begin{bmatrix} [\boldsymbol{U}]_a \\ [\boldsymbol{U}]_c \\ [\boldsymbol{U}]_b \end{bmatrix}, \qquad {}_{AB}[\boldsymbol{H}] = \begin{bmatrix} [\boldsymbol{H}]_{aa} & [\boldsymbol{H}]_{ac} & [\boldsymbol{H}]_{ab} \\ [\boldsymbol{H}]_{ca} & [\boldsymbol{H}]_{cc} & [\boldsymbol{H}]_{cb} \\ [\boldsymbol{H}]_{ab} & [\boldsymbol{H}]_{bc} & [\boldsymbol{H}]_{bb} \end{bmatrix}, \qquad {}_{AB}[\boldsymbol{F}] = \begin{bmatrix} [\boldsymbol{F}]_a \\ [\boldsymbol{F}]_c \\ [\boldsymbol{F}]_b \end{bmatrix} \tag{14}$$

The receptance matrix ${}_{AB}[\boldsymbol{H}]$ cannot be determined directly from the receptance matrices of the subsystems. Two natural conditions must be verified in the coupling method, imposing the compatibility condition at the interface and equality with opposite signs of the forces. The FRFs of the coupling DoFs between two subsystems $A$ and $B$ were expressed as in [22].

$$\begin{aligned} {}_{AB}[\boldsymbol{H}] &= \begin{bmatrix} {}_A[\boldsymbol{H}] & \boldsymbol{0} \\ \boldsymbol{0} & {}_B[\boldsymbol{H}] \end{bmatrix} - \begin{bmatrix} {}_A[\boldsymbol{H}]_{ic} \\ {}_A[\boldsymbol{H}]_{cc} \\ {}_B[\boldsymbol{H}]_{jc} \end{bmatrix} ({}_A[\boldsymbol{H}]_{cc} + {}_B[\boldsymbol{H}]_{cc})^{-1} \begin{bmatrix} {}_A[\boldsymbol{H}]_{ic} \\ {}_A[\boldsymbol{H}]_{cc} \\ {}_B[\boldsymbol{H}]_{jc} \end{bmatrix}^{\mathrm{T}} \\ {}_A[[\boldsymbol{H}]] &= \begin{bmatrix} {}_A[\boldsymbol{H}]_{ii} & {}_A[\boldsymbol{H}]_{ic} \\ {}_A[\boldsymbol{H}]_{ci} & {}_A[\boldsymbol{H}]_{cc} \end{bmatrix}, \qquad {}_B[\boldsymbol{H}] = [{}_B[\boldsymbol{H}]_{jj}] \end{aligned} \tag{15}$$

where ${}_{AB}[\boldsymbol{H}]$ represents the FRF matrix of the assembled system. ${}_A[\boldsymbol{H}]$ and ${}_B[\boldsymbol{H}]$ are the FRF matrices of subsystems $A$ and $B$, respectively. Subscripts $i$ and $j$ represent the internal DoFs and $c$ denotes the coupling DoFs. Eq. (15) is used to calculate the global system coupling FRF. For the flexible joint, the Kernel matrix $({}_A[\boldsymbol{H}]_{cc} + {}_B[\boldsymbol{H}]_{cc})^{-1}$ in Eq. (15) must be replaced by $({}_A[\boldsymbol{H}]_{cc} + {}_B[\boldsymbol{H}]_{cc} + {}_B[\boldsymbol{K}]_s^{-1})$, where ${}_B[\boldsymbol{K}_s]$ is the coupling stiffness matrix between the coupling DoFs of both subsystems [26]. The two FBS formulation subsystems limitation is generalized in [36].

### 3.2. Determination of the FRF

The first step in the analytical FBS procedure is the determination of the FRFs. Moreover the driving points FRFs in the coupling points are essential for the FBS procedure. Using a Fourier transformation, the subsystem dynamic behavior can be expressed in the frequency domain. The format of the motion equations in the frequency domain depends on the physical quantity of the response parameter (i.e. displacement, velocity or acceleration) that is used in the analysis. Classically, the motion equation is written in displacement, which leads to:

$$\{\boldsymbol{X}(\omega)\} = [\boldsymbol{H}(\omega)]\{\boldsymbol{F}(\omega)\}, \qquad [\boldsymbol{H}(\omega)]^{-1} = [\boldsymbol{K}] - \omega^2[\boldsymbol{M}] + \mathrm{j}\,\omega[\boldsymbol{C}] \tag{16}$$

The FRF of a mechanical system can be determined by performing an FRF synthesis based on a finite number of mode shapes and natural frequencies. For proportionally damped systems, this relationship between the FRF matrix $H_{jk}(\omega)$ and mode shapes is expressed by:

$$\boldsymbol{H}_{jk}(\omega) = \sum_{r=1}^{n} \frac{r_{\Phi_j} r_{\Phi_k}}{\omega_r^2 - \omega^2 + 2\,\mathrm{j}\,\xi_r \omega_r \omega} \tag{17}$$

where $\boldsymbol{H}_{jk}(\omega)$ is the steady-state displacement at coordinate $j$ due to a harmonic force excitation at coordinate $k$. $n$ denotes the DoFs. $r_{\Phi_j}$ is the mass-normalized eigenvector of the physical coordinate $j$ and the mode number $r$.

### 3.3. The dynamic condensation

The coupled system $AB$ can be divided as follows [25]:

$${}_{AB}[\boldsymbol{H}] = \begin{bmatrix} {}_{AB}[\boldsymbol{H}]_{MM} & {}_{AB}[\boldsymbol{H}]_{MS} \\ {}_{AB}[\boldsymbol{H}]_{SM} & {}_{AB}[\boldsymbol{H}]_{SS} \end{bmatrix} = \begin{bmatrix} [\boldsymbol{H}]_{aa} & [\boldsymbol{H}]_{ac} & [\boldsymbol{H}]_{ab} \\ [\boldsymbol{H}]_{ca} & [\boldsymbol{H}]_{cc} & [\boldsymbol{H}]_{cb} \\ [\boldsymbol{H}]_{ba} & [\boldsymbol{H}]_{bc} & [\boldsymbol{H}]_{bb} \end{bmatrix} \tag{18}$$

According to Eq. (31), the condensed receptance matrix of the coupled system $AB$ becomes:

$$\begin{aligned} {}_{AB}[\boldsymbol{H}] &= \begin{bmatrix} [\boldsymbol{H}]_{aa} & [\boldsymbol{H}]_{ac} \\ [\boldsymbol{H}]_{ca} & [\boldsymbol{H}]_{cc} \end{bmatrix} - \begin{bmatrix} [\boldsymbol{H}]_{ab} \\ [\boldsymbol{H}]_{cb} \end{bmatrix} [\boldsymbol{H}]_{bb}^{-1} \begin{bmatrix} [\boldsymbol{H}]_{ba} & [\boldsymbol{H}]_{bc} \end{bmatrix} \\ &= \begin{bmatrix} [\boldsymbol{H}]_{aa} - [\boldsymbol{H}]_{ab}[\boldsymbol{H}]_{bb}^{-1}[\boldsymbol{H}]_{ba} & [\boldsymbol{H}]_{ac} - [\boldsymbol{H}]_{ab}[\boldsymbol{H}]_{bb}^{-1}[\boldsymbol{H}]_{bc} \\ [\boldsymbol{H}]_{ca} - [\boldsymbol{H}]_{cb}[\boldsymbol{H}]_{bb}^{-1}[\boldsymbol{H}]_{bc} & [\boldsymbol{H}]_{cc} - [\boldsymbol{H}]_{cb}[\boldsymbol{H}]_{bb}^{-1}[\boldsymbol{H}]_{bc} \end{bmatrix} \end{aligned} \tag{19}$$

with $[\boldsymbol{H}]_{ab} = 0$, ${}_{AB}[\boldsymbol{H}] = \begin{bmatrix} [\boldsymbol{H}]_{aa} & [\boldsymbol{H}]_{ac} \\ [\boldsymbol{H}]_{ca} & [\boldsymbol{H}]_{cc} - [\boldsymbol{H}]_{cb}[\boldsymbol{H}]_{bb}^{-1}[\boldsymbol{H}]_{bc} \end{bmatrix}$.

The condensed receptance matrix of the coupled system $AB$ can be also expressed by:

$${}_{AB}[\boldsymbol{H}] = \begin{bmatrix} [\boldsymbol{H}]_{cc} & [\boldsymbol{H}]_{cb} \\ [\boldsymbol{H}]_{bc} & [\boldsymbol{H}]_{bb} \end{bmatrix} - \begin{bmatrix} [\boldsymbol{H}]_{ca} \\ [\boldsymbol{H}]_{ba} \end{bmatrix} [\boldsymbol{H}]_{aa}^{-1} \begin{bmatrix} [\boldsymbol{H}]_{ac} & [\boldsymbol{H}]_{ab} \end{bmatrix} \tag{20}$$

According to Eq. (31), the condensed receptance matrix of the subsystems $A$ and $B$ are expressed by:

$${}_{A}[\boldsymbol{H}] = [\boldsymbol{H}]_{aa} - [\boldsymbol{H}]_{ac} \left([\boldsymbol{H}]_{cc} - [\boldsymbol{H}]_{cb}[\boldsymbol{H}]_{bb}^{-1}[\boldsymbol{H}]_{bc}\right)^{-1} [\boldsymbol{H}]_{ca} \tag{21}$$

$${}_{B}[\boldsymbol{H}] = [\boldsymbol{H}]_{bb} - [\boldsymbol{H}]_{bc} \left([\boldsymbol{H}]_{cc} - [\boldsymbol{H}]_{ca}[\boldsymbol{H}]_{aa}^{-1}[\boldsymbol{H}]_{ac}\right)^{-1} [\boldsymbol{H}]_{cb} \tag{22}$$

## 4. Numerical simulations and discussions

Numerical simulations based on a coupling method are used to study the vibration behavior of the spur gear system powered by different subsystems. Damping is neglected in this model. The natural frequencies of each subsystem are validated with reference to the literature. The substructure coupled FRF is compared to the global system FRF to prove the performance of the substructuring method. The Frequency Response Function and the coupling methods are used to calculate the transfer functions of each subsystem and of the global system. The parallel stage and the planetary gear are analyzed separately. This analysis is focused on the modes shapes and corresponding frequencies calculation. The eigenmodes and the FRF using both models are compared to the present method. The mechanical parameters of the studied system are given in Tables 1 and 2.

### 4.1. Validation of the substructuring method

The studied example is based on a synthesis of the work presented by Kahraman on parallel gear and Parker on planetary gear. The example of the planetary gear stage with four planets was chosen by Lin and Parker [33]. The resolution of the eigenproblem allows recovering the eigenfrequencies of both subsystems. The eigenfrequencies of parallel gears were compared to Kahraman's results. A good accuracy between the two results was evidenced. It is assumed that the FRF receptance $H$ describing the displacement/force for each subsystem is known. Fig. 3 depicts the FRF of a parallel stage. $H_{yy}$ and $H_{zz}$ present the receptance magnitude of subsystem $A$ in radial and axial directions. The natural frequencies are computed in the frequency range [0–4000] Hz, with a step of 1 Hz. The presented peaks correspond to the natural frequencies of subsystem $A$. These peaks present the rotation and the bending modes.

The planetary gear model introduced by Lin and Parker [33] was used to verify the present results. These results were compared to the published frequency analysis [33] of planetary gear sets with various numbers of planet gears. The natural frequencies and their multiplicities for different numbers of planets $N = 3, 4, 5$ were proven. The natural frequencies of the planetary system were classified according to [33]. These frequencies indicate the vibration modes in three types: translational modes in which the sun, the carrier, and the ring have only a translational motion; rotational modes in which the sun, the carrier, and ring have only rotational motion around the rotation axis; and planet modes in which the sun, carrier, and the ring are fixed. The frequency response analysis was computed to estimate the vibration behavior of the

**Table 1**
The parameters of the parallel stage ($i = 1, 2$).

| | |
|---|---|
| Wheel and pinion mass (kg) | $m_i = 2$ |
| Wheel and pinion inertia moment (kg) | $I_i/(r_i)^2 = 0.58$ |
| Wheel and pinion inertia moment (kg) | $J_i/(r_i)^2 = 1.16$ |
| Bearings stiffness (N/m) | $k_{yi} = 3.5 \times 10^8$, $k_{zi} = 10^8$ |
| Torsional shaft flexibilities (N/m) | $k_{b\rho yi}/(r_i)^2 = 10^8$ |
| Pressure angle | $\alpha_1 = \alpha_2 = 20°$ |
| Teeth module (m) | $m = 4 \times 10^{-3}$ |
| Average mesh stiffness (N/m) | $k_{1\text{moy}} = k_{2\text{moy}} = 2 \times 10^8$ |
| Inertia coupling (kg m$^2$) | $I_A = 4.48 \times 10^{-8}$ |

**Table 2**
The planetary gear parameters.

| | Sun | Ring | Carrier | Planet |
|---|---|---|---|---|
| Teeth number | 30 | 70 | – | 20 |
| Module | 1.7 | 1.7 | | 1.7 |
| Teeth width (mm) | 25 | 25 | | 25 |
| Mass (kg) | 0.46 | 0.588 | 3 | 0.177 |
| $I/r^2$ (kg) | 0.272 | 0.759 | 1.5 | 0.1 |
| Base radius (m) | 0.024 | 0.056 | – | 0.016 |
| Helix angle (°) | 0 | 0 | | 0 |
| Gear mesh stiffness (N/M) | $K_{sp} = K_{rp} = 2{\cdot}10^8$ | | | |
| Bearing stiffness (N/m) | $K_p = K_{su,v} = K_{ru,v} = 10^8$ | | | |
| Torsional (N/m) | $k_{rw} = 10^9$; $K_{sw} = 10^5$; $K_{cw} = 0$ | | | |
| Pressure angle (°) | $s = r = 21.34$ | | | |

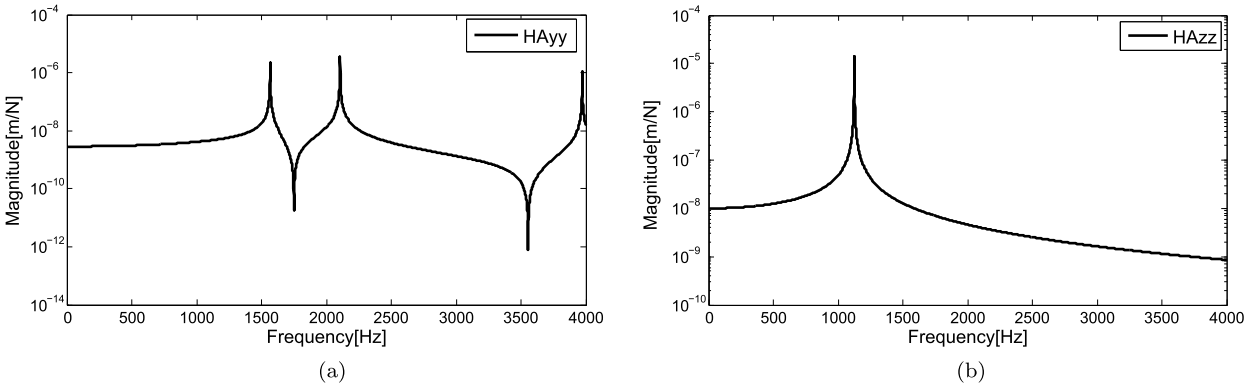


(a) (b)

**Fig. 3.** Subsystem $A$ FRF in axial and radial directions: (a) in direction $y$ and (b) in direction $z$.

planetary gear system. Fig. 4 depicts the FRF of the planetary gear with four planet gears in radial and rotational directions. The natural frequencies were computed in the frequency range [0–15000] Hz, with a 10 Hz step. The presented peaks correspond to the natural frequencies of subsystem $B$. The receptance magnitude $H_{11}$ is given in Eq. (15). $H_{11}$ is the translational FRF in the radial direction $u$, which is the sun DoF on subsystem $B$.

Next, the two subsystems $A$ and $B$ were coupled using the substructuring method. This analysis is focused on the calculation of the full-system FRF using the two methods. The transfer functions obtained by both methods were compared and the effect of the stiffness value on the substructuring method is discussed. The natural frequencies obtained by the full-system method correspond to the natural frequencies of the subsystem denoted as an individual stage (Table 3). The changed modes are classified as global modes. The global system modes can be partitioned into parallel stage modes, planetary gear modes, and global modes. The parallel stage output shaft follows the rotation of the sun input of the planetary stage. The shaft stiffness value of the sun is taken as $k_{sw} = 10^5$ N/m. For the planetary stage, some natural frequencies remain identical to the those in the subsystem analysis, when coupled with the parallel stage.

The receptance of the system $AB$ is obtained using the procedure described in section 3. The FRF results of system $AB$ using the coupling procedure and the full-system FRF are shown in Figs. 5–7.

Fig. 5 displays an FRF comparison using two methods in the radial and rotational directions $u$ and $w$ of the sun. The coupled method FRF curves were calculated from the FRF via Eq. (15). By coupling the first parallel with the second planetary gear stage, we obtain FRF results that agree with those of the full-system FRF. The two curves obtained by the coupled substructure and the full system FRF methods are identical. The natural frequencies obtained by the two methods are in good agreement. Besides, the simplicity of the coupling method reduces the computational time by 70% compared to the

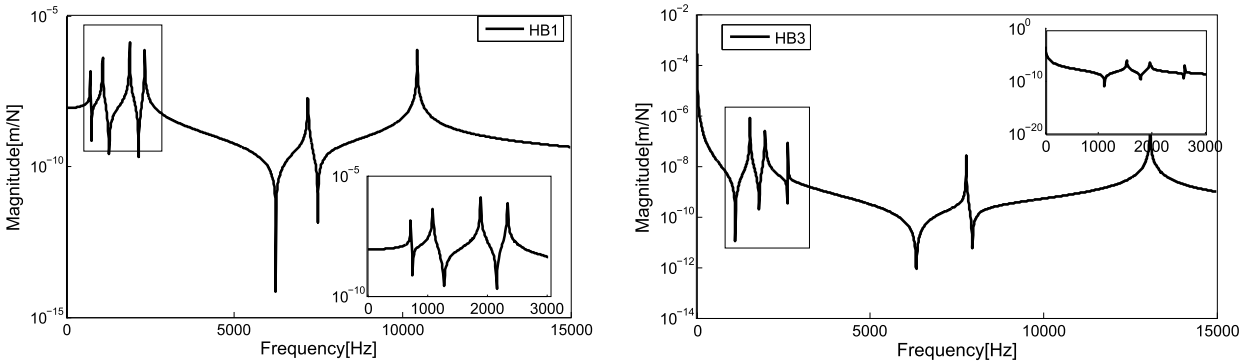


**Fig. 4.** Subsystem $B$ FRF: (a) in the radial direction $u$ and (b) in the rotational direction $w$ of the sun.

**Table 3**
Full system natural frequencies.

| $N$ | Global mode | Planetary stage | | | Parallel stage |
|---|---|---|---|---|---|
| | | Rotational mode | Translational mode | Planet mode | |
| 1 | | 0 | | | |
| 2 | 71 | | | | |
| 3 | | | 727(2) | | |
| 4 | | | 1091(2) | | |
| 5 | | | | | 1125(2) |
| 6 | | 1537 | | | |
| 7 | | | | | 1566 |
| 8 | | | | 1808 | |
| 9 | | | 1893(2) | | |
| 10 | | 1971 | | | |
| 11 | | | | | 2105 |
| 12 | | | | | 2202 |
| 13 | | | 2343(2) | | |
| 14 | | 2626 | | | |
| 15 | | | | | 3972 |
| 16 | | | | 5964 | |
| 17 | | | | 6981 | |
| 18 | | | 7190(2) | | |
| 19 | | 7774 | | | |
| 20 | | 10438(2) | | | |

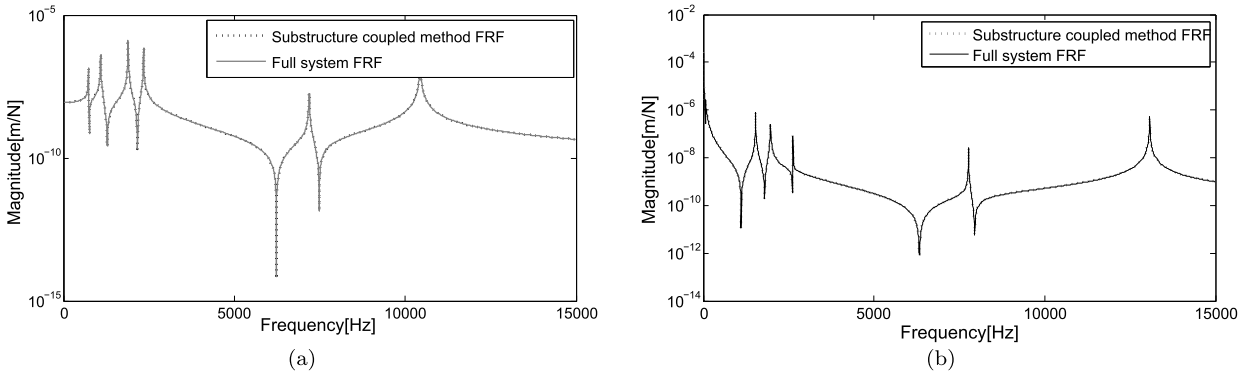


**Fig. 5.** Coupled system FRF computed by two methods: (a) in the radial direction $u$, (b) in the rotational direction $w$ of the sun.

full-system FRF. $H_{cc}$ denotes the coupling receptance magnitude described in Eq. (15). Fig. 6(a) depicts the receptance magnitude $H_{99}$ of the indirect and direct methods of the coupling torsion degree. The natural frequencies obtained by the coupled substructure and those obtained by the full system FRF methods are in a good agreement. Fig. 6(b) depicts the receptance magnitude $H_{1313}$ in the DoF 13 radial direction corresponding to the planetary modes. $H_{cb}$ presents the coupling receptance magnitude between the coupling degree and the internal degrees of subsystem $B$, which is presented in Eq. (15).

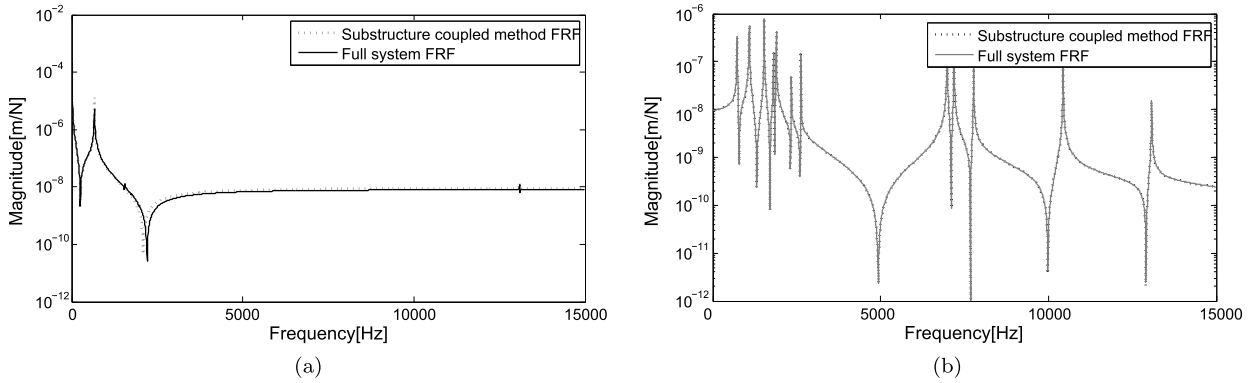


**Fig. 6.** Coupled system FRF: (a) $H_{99}$ at the coupling DoF $\theta(2,2)$, (b) $H_{13-13}$ at the degree of the second planet $u_{p2}$ in the radial direction.

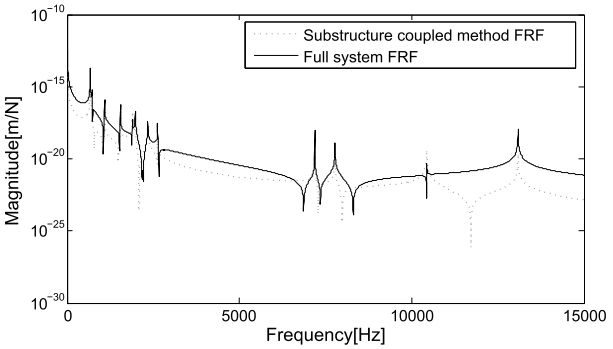


**Fig. 7.** The FRF $H_{910}$ coupling between the coupling DoF $\theta(2,2)$ and the degree of the sun $u_s$.

Fig. 7 depicts the receptance magnitude $H_{12}$ in the indirect method where index 1 correspond to the coupling DoF of $B$, the index 2 is the sun DoF in the radial direction and $H_{910}$ in the direct method where 9 represents the coupling DoF and 10 represents the sun DoF. The results obtained by the two methods are in good agreement for all the frequencies, except a small difference in magnitude. The substructuring method accuracy is also noticed in the transfer functions apart from the diagonal one. In order to validate the two methods, all the FRFs of the coupled system were investigated by comparing them to the full-system FRFs. A good agreement is presented for all FRFs. Some of the achieved results are presented in Figs. 5–7 for different DoFs.

### *4.2. Stiffness effect on the substructuring method*

The effect of shaft stiffness on the coupling method is analyzed in this section. Figs. 8 and 9 present the effect of the shaft coupling stiffness on the substructuring method in the radial and rotational directions of the sun. This effect was studied for three different shaft stiffness value $k_{sw} = 10^5, 10^6$, and $10^7$ N/m. The studied cases of the sun's radial direction are presented in Fig. 8a–c. The obtained results using the coupled FRF and the full FRF methods are similar in the frequency range [0–15000] Hz. By coupling the parallel stage with the planetary gear system, the same frequencies are found in both methods. Nevertheless, a small difference appears in their magnitudes. This difference becomes considerable for an increased stiffness of the transnational modes (see Fig. 8c). Fig. 8c depicts the appearance of a new frequency in the coupled method FRF. This difference is sensitive to shaft stiffness. The new frequency is not present for the second radial displacement FRF. Nevertheless, with decreasing shaft stiffness, the difference in magnitude became small, as shown in Fig. 8a–b. Both magnitude and natural frequencies are sensitive to stiffness. The difference in frequencies increased with shaft stiffness (see Fig. 9a–b). The coupled FRF curve is slightly higher than the full FRF curve at some frequencies. The natural frequencies of the overall system in substructure method are sensitive to the coupling stiffness. The rotational modes of subsystem $B$ computed using the full system and the coupling FRF, are shown in Table 4. The achieved results explain the frequency that appeared in the rotational modes. The natural frequencies obtained by the coupled substructure FRF and those obtained by the full system FRF methods are in good agreement in rotational degrees. In two radials directions of the planetary gear, some new frequencies appeared. For a decreased stiffness, the rotational mode shift frequency also decreased. The substructuring method is sensitive to the shaft stiffness attached to the coupling.

The eigenfrequencies of subsystem $B$ shift to a lower frequency when using the coupling method of the system $AB$. This difference appears in rotational modes.

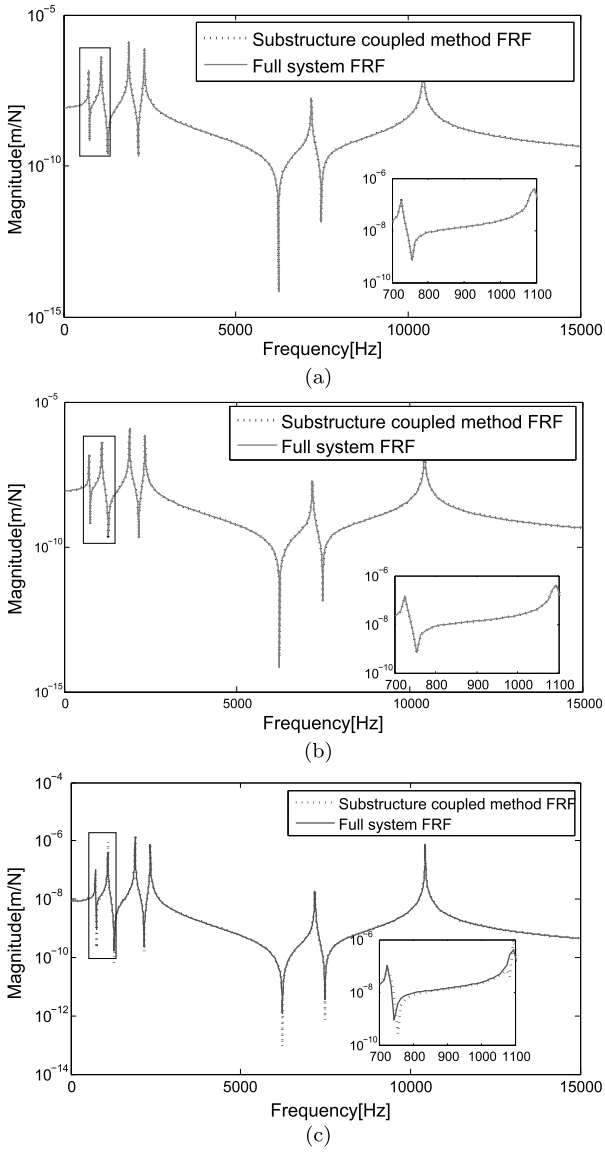


**Fig. 8.** The sun's radial FRF direction: (a) $k_{sw} = 10^5$, (b) $k_{sw} = 10^6$, and (c) $k_{sw} = 10^7$.

**Table 4**
Comparison of the rotational modes.

| Full-system rotational mode in the FRF | Coupling method rotational mode in the FRF |
|---|---|
| 0 | 0 |
| 1550 | 1537 |
| 1982 | 1971 |
| 2626 | 2626 |
| 7774 | 7774 |
| 10438 | 10438 |

### *4.3. Condensation method effect on subsystems A and B*

In this section, the sensitivity of the condensation on the substructuring method was discussed. The FRF of each subsystem was computed in the frequency range [0–4000] Hz. Fig. 10 depicts the FRF results of the condensed subsystem $A$ in $AB$ and the FRF of non-condensed subsystem $A$ in the radial and rotational directions. The two curves obtained by the condensed and non-condensed methods were superposed in the radial direction (see Fig. 10a). Nevertheless, a small differences appears in Fig. 10b in frequency and magnitude in the rotational direction. The peak located around 2000 Hz

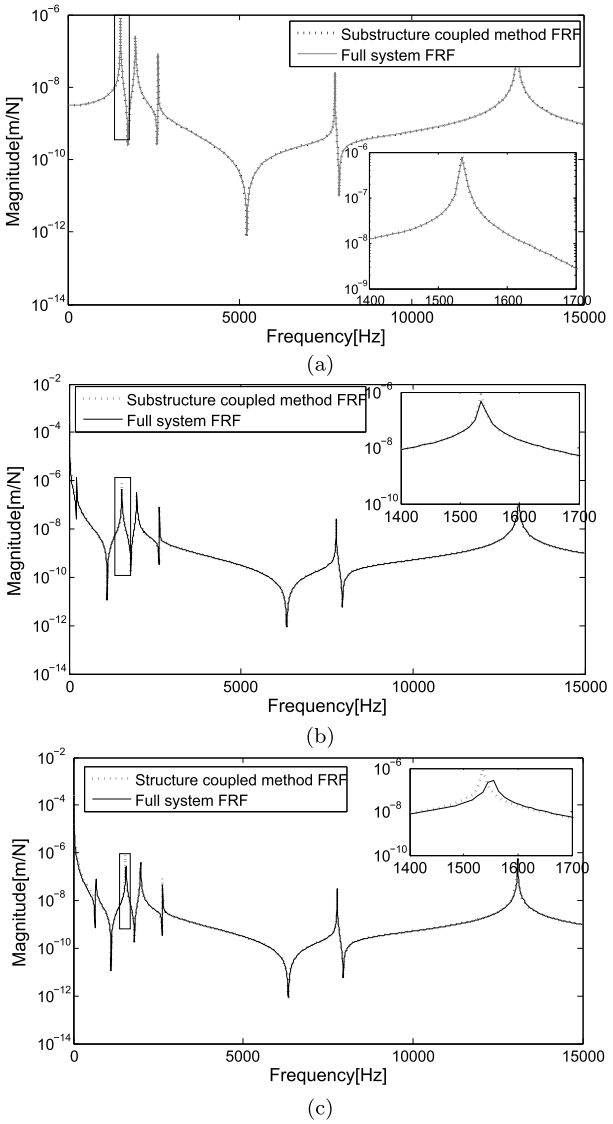


**Fig. 9.** The sun's rotational FRF direction: (a) $k_{sw} = 10^5$, (b) $k_{sw} = 10^6$ and (c) $k_{sw} = 10^7$.

shifts rearward in the condensed subsystem under the effect of subsystem $B$. The peak appearing at around 70 Hz is due to the coupling DoF. The difference in magnitude and natural frequencies of subsystem $A$ between the condensed and the non-condensed methods is due to the neighbor effects of the subsystem $B$ and the coupling. The FRF of subsystem $A$ in the rotational direction is sensitive to the neighboring subsystem $B$ and coupling DoF.

The FRF of subsystem $B$ in $AB$ and the FRF of subsystem $B$ separately are shown in Fig. 11. A new frequency has clearly appeared, corresponding to the coupling frequency. In the radial direction, the condensed and the non-condensed FRF of subsystem $B$ are superposed (see Fig. 11a). The neighbor subsystem $A$ is not affected by the receptance of subsystem $B$. Subsystem $B$ FRF is sensitive to the coupling DoF. The reducer subsystem $A$ FRF is more sensitive to condensation than the planetary subsystem $B$ FRF.

The effect of stiffness on neighbor subsystems $A$ and $B$ was analyzed in this section using the condensation method. Fig. 12 shows a comparison between the condensed and the non-condensed FRF in the rotational direction of subsystem $B$ by varying shaft stiffness. The two curves in each figure are not superposed; a difference in frequencies and magnitude appeared. The frequencies that appeared in the condensed subsystem $A$ in Fig. 12a shift to low frequencies in the case of a decreased stiffness value (see Fig. 12b). The difference in the FRF of the condensed and the non-condensed subsystem $A$ is due to the effect of subsystem $B$ (different transmission). Subsystem $A$ FRF is sensitive to the subsystem $B$ FRF. The appearance of some peaks in the FRF of the condensed subsystem $A$ is due to the neighbor system.

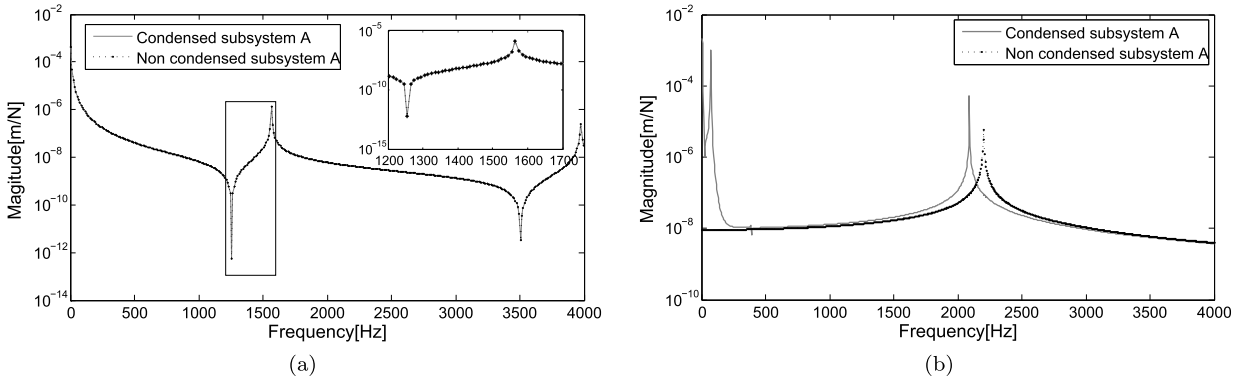


**Fig. 10.** Condensed and non-condensed subsystem *A* FRF: (a) in the radial direction, (b) in the rotational direction.

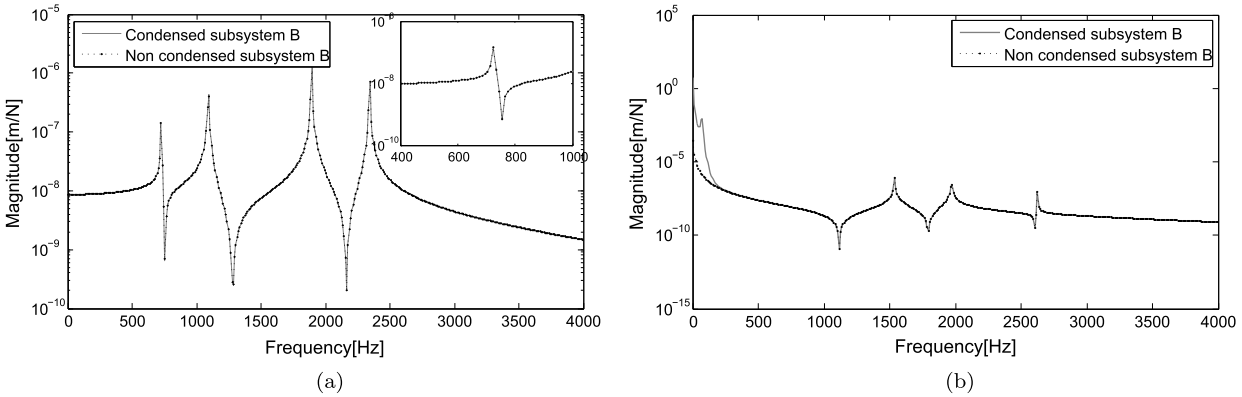


**Fig. 11.** Condensed and non-condensed subsystem *B* FRF: (a) in the radial direction, (b) in the rotational direction.

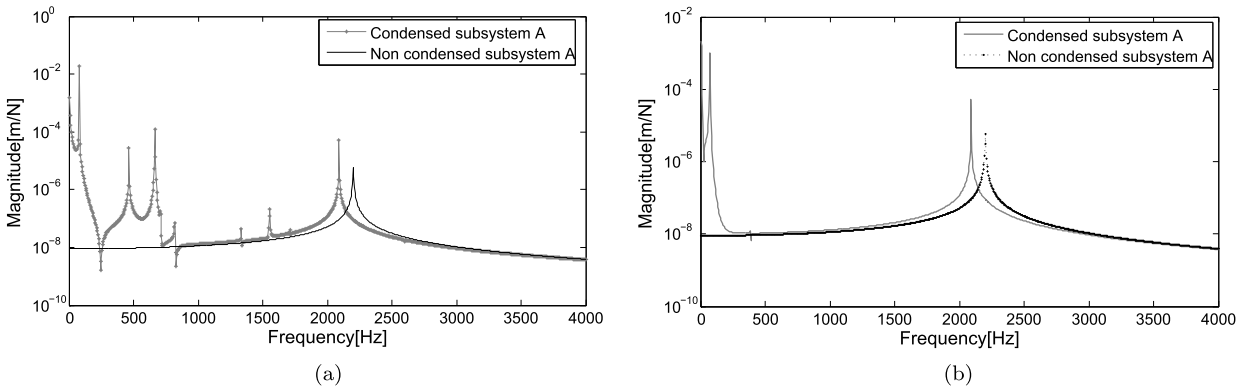


**Fig. 12.** Condensed and non-condensed subsystem *A* FRF in the rotational direction of the sun: (a) $k_{sw} = 10^7$, (b) $k_{sw} = 10^5$.

### *4.4. Modal truncation influence on the planetary and reducer systems FRF*

In this section, the effect of modal truncation was investigated by decreasing the number of modes taken into account. The interest frequency range is assumed to be between 0 and 4000 Hz, and the corresponding response models are generated by truncating each mode. The FRF of subsystem *B* without truncation is compared to the truncated FRF by considering only the frequencies inside the range [0–4000] Hz. The analysis of the modal truncation was investigated mode by mode until the last nine modes outside of the frequency range. The curves of the truncated FRF of subsystem *B* from one to nine modes are superposed in Fig. 13 in the radial and rotational directions. On the one hand, a small difference in frequencies and magnitude between the FRF of subsystem *B* without truncation and the FRF truncated was shown. On the other hand, the two curves are superposed in the two studied cases, which are the coupling mode and the last nine modes outside the frequency range. It can be concluded that the coupling mode is sensitive to the modal truncation approach. Truncated high

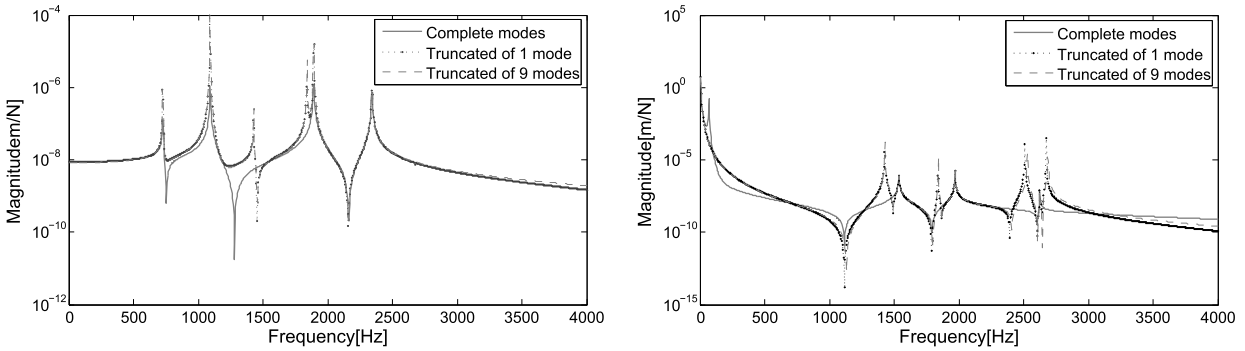


**Fig. 13.** FRF of the truncated and non-truncated subsystem $B$: (a) in the translational, (b) in the rotational direction of the sun.

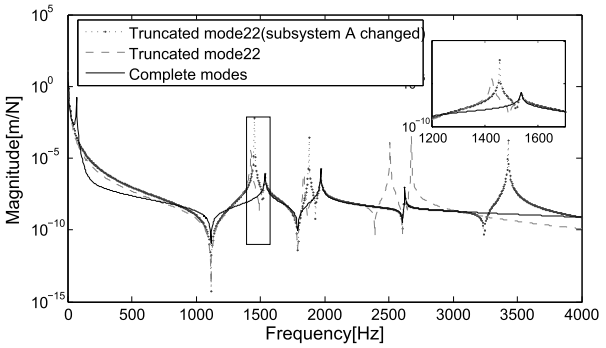


**Fig. 14.** The FRF of truncated subsystem $B$.

modes affect the FRF results of subsystem $B$. The FRF of subsystem $B$ is sensitive to the modal truncation, depending on how many and which modes are truncated [30]. The appearance of some frequencies around 1400, 1800, 2500, and 2650 Hz in the radial and rotational directions function FRF is due to the modal modes selected. It depends on unmeasured coupling DoF (see Fig. 15) and the frequency of subsystem $A$ due to the dynamic condensation equation.

Some peaks appear in Fig. 13, corresponding to the frequencies of subsystem $A$. Fig. 14 shows that the parameters of subsystem $A$ affect the FRF of the truncated subsystem $B$. The FRF of subsystem $B$ with the truncated coupling mode and the sun shaft stiffness change is compared with the FRF of the truncated subsystem $B$ without changing the stiffness of subsystem $A$. The difference in the frequencies between both FRFs is shown in Fig. 13. The FRF of subsystem $B$ is sensitive to the shaft stiffness of subsystem $A$. Except the coupling mode, the truncation of modes outside the frequency range does not affect the FRF response in the translational and rotational directions. The truncated FRF is sensitive to the connection DoF. The truncated 9 modes do not affect the FRF response.

The effect of truncation on the FRF of subsystem $B$ without condensation was investigated. Fig. 15 depicts a comparison between the FRF of subsystem $B$ without and with all truncated modes located beyond 4000 Hz. All the obtained curves without and with modal truncation were superposed for all the frequencies in the rotational direction. No effect appears on the truncated FRF of subsystem $B$ in the rotational direction (see Fig. 15a). But the effect is observed in Fig. 15b, so the coupling degree FRF is sensitive to the coupling truncation degree. The modal truncation is sensitive to the FRF of subsystem $B$ in the range of interest.

Fig. 16 depicts the FRF of subsystem $A$ without and with the truncated mode of subsystem $B$ outside the frequency range. The effect of truncated mode of subsystem $B$ on the FRF of subsystem $A$ is presented in radial and rotational directions. Fig. 16(a) shows some difference in frequencies between the two curves without truncation and with the coupling degree truncation. Nevertheless, FRF in the radial direction is not sensitive to truncation. Also the truncated of all modes outside the frequency range corresponds to the same difference as the coupling mode truncation. Some clearly seen peaks correspond to the rotational frequency of subsystem $B$. The frequencies of subsystem $B$ are shown in the FRF of subsystem $A$ when truncating the coupling DoF. It should be noticed that the truncated coupling mode affects the FRF of subsystem $B$.

As a conclusion on modal truncation, all modes outside of the frequency range except the coupling DoF can be neglected. The modal truncation does not affect the substructuring method outside the frequency range. The modal truncation affects the transmission reducer and the planetary system. The truncation mode of $B$ on the FRF of subsystem $A$ is more sensitive than on the FRF of subsystem $B$. The use of the modal truncation leads to results whose accuracy depends on the selected eliminated modes. The choice of the truncated modes should be carried out according to the higher modes. The FRF is

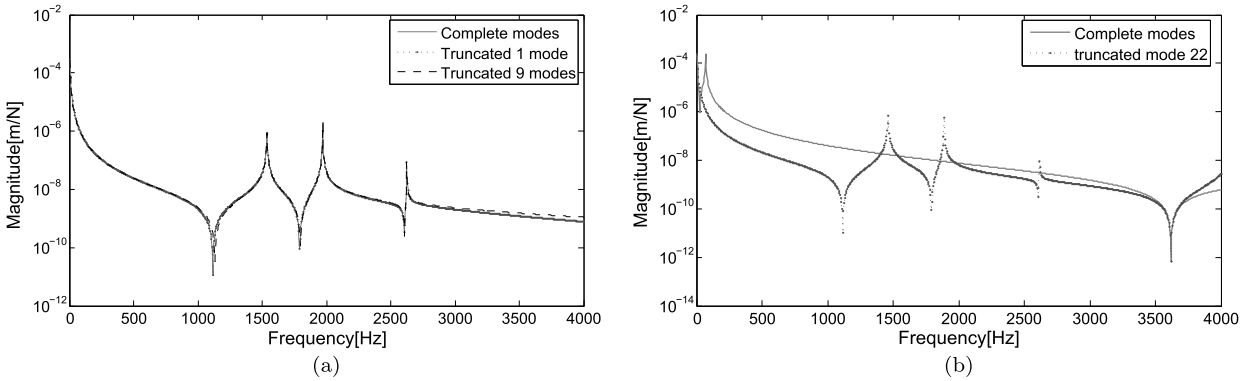


**Fig. 15.** The FRF of truncated modal of subsystem $B$ without condensation: (a) in the rotational direction, (b) in the direction of the coupling DoF.

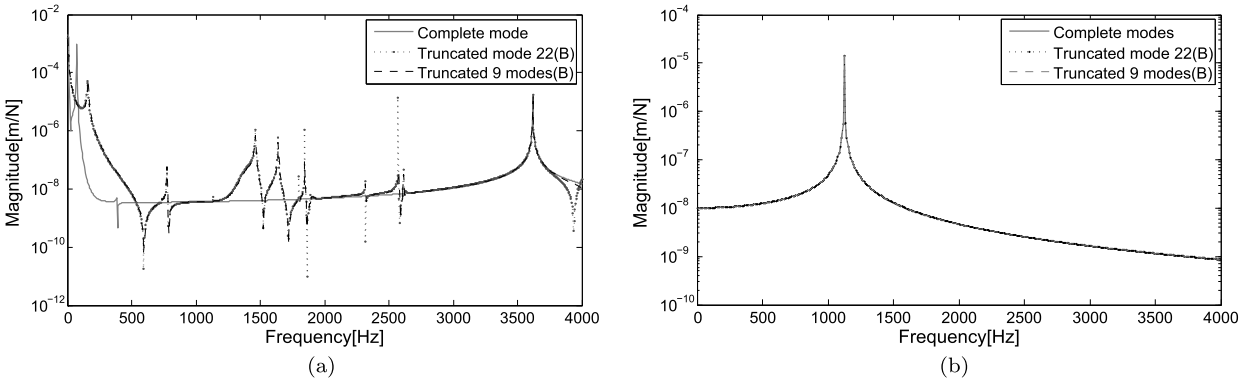


**Fig. 16.** Truncated subsystem $A$: (a) in the rotational direction, and (b) in the radial direction.

sensitive to the coupling DoF truncation. In contrast, other modes truncated outside the frequency range of interest preserve the dynamic properties of the two subsystems $A$ or $B$.

## 5. Conclusions

The present work is based on substructuring method of two rigid connected transmission subsystems, which are the parallel stage and the planetary gear system. The FRF of each subsystem was determined separately and then the coupled system is obtained using the coupling method. To verify the coupling procedures, the results were compared to those of the full system. It is observed that the natural frequencies obtained by the FRF of the global system and those of the coupled system are in good agreement. However, a small difference appears in magnitude and frequency, which is due to the shafts stiffness. The effect of shaft stiffness on the substructuring method is investigated. It was noted that the coupling method reduces the computational time compared to the FRF of the full system. The effect of coupling and neighboring subsystems is shown in the condensed method. The substructure method was verified by comparing the solutions obtained by truncating all modes located outside the analyzed frequency range to the corresponding solutions obtained by the direct approach. The solutions obtained through modal truncation are superposed on exact solutions for a direct comparison, except in the coupling mode. The FRF of each subsystem is sensitive to the coupling DoF truncation.

## Appendix A. Stiffness and mass matrix of subsystem *B*

The bearings stiffness matrix $\mathbf{K}_{bB}$ is written as:

$$\mathbf{K}_{bB} = \begin{bmatrix} \mathbf{K}_{sb} & 0 & 0 \\ 0 & \mathbf{K}_{cb} & 0 \\ 0 & 0 & \mathbf{K}_{rb} \end{bmatrix} \tag{23}$$

where $\mathbf{K}_{sb} = \begin{bmatrix} 0 & 0 & 0 & 0 \\ 0 & K_{su} & 0 & 0 \\ 0 & 0 & K_{sv} & 0 \\ 0 & 0 & 0 & 0 \end{bmatrix}$, $\mathbf{K}_{jb} = \begin{bmatrix} K_{ju} & 0 & 0 \\ 0 & K_{jv} & 0 \\ 0 & 0 & K_{jw} \end{bmatrix}$, $j = r, c.$

$K_{ju}$, $K_{jv}$, $K_{jw}$ are the bearing stiffnesses along the tree degree of freedom.
The shaft stiffness matrix $\mathbf{K}_{ss}$ is written as:

$$\mathbf{K}_{ss} = [K_{ss1}, \text{zeros}(4, 18); \text{zeros}(6, 22); \text{zeros}(3n, 10), \text{zeros}(3n, 3n)] \tag{24}$$

where $K_{ss1} = \begin{bmatrix} K_{sw} & 0 & 0 & -K_{sw} \\ 0 & 0 & 0 & 0 \\ 0 & 0 & 0 & 0 \\ -K_{sw} & 0 & 0 & K_{sw} \end{bmatrix}$.

The matrix of the mean gear stiffness $\mathbf{K}_{mB}$ is written as:

$$\mathbf{K}_{mB} = \begin{bmatrix} \sum K_{s1}^n & 0 & 0 & K_{s2}^1 & \dots & K_{s2}^n \\ 0 & \sum K_{c1}^n & 0 & K_{c1}^1 & \dots & K_{c2}^n \\ 0 & 0 & \sum K_{r1}^n & K_{r1}^1 & \dots & K_{r2}^n \\ K_{s2}^1 & K_{c2}^1 & K_{r2}^1 & K^1 & 0 & 0 \\ \vdots & \vdots & \vdots & \vdots & \ddots & \\ K_{s2}^N & K_{c2}^N & K_{r2}^N & 0 & 0 & K^N \end{bmatrix} \tag{25}$$

$$K_{c1}^n = kp \begin{bmatrix} 1 & 0 & -\sin\varphi_p \\ 0 & 1 & \cos\varphi_p \\ -\sin\varphi & \cos\varphi_p & 0 \end{bmatrix}$$

$$K_{r1}^n = krp \begin{bmatrix} \sin^2\varphi_{rp} & -\cos\varphi_{rp}\cos\alpha_r & \sin\varphi_{rp} \\ -\cos\varphi_{rp}\cos\alpha_r & \cos^2\varphi_{rp} & \cos\varphi_{rp} \\ \sin\varphi_{rp} & \cos\varphi_{rp} & 1 \end{bmatrix}$$

$$K_{s1}^n = ksp \begin{bmatrix} 0 & 0 & 0 & 0 \\ 0 & \sin^2\varphi_{sp} & -\cos\varphi_{sp}\cos\alpha_s & -\sin\varphi_{sp} \\ 0 & -\cos\varphi_{sp}\cos\alpha_s & \cos^2\varphi_{sp} & \cos\varphi_{sp} \\ 0 & -\sin\varphi_{sp} & \cos\varphi_{sp} & 1 \end{bmatrix}$$

$$K_{c2}^N = kp \begin{bmatrix} -\cos\varphi_p & \sin\varphi_p & 0 \\ -\sin\varphi_p & -\cos\varphi_p & 0 \\ 0 & 1 & 0 \end{bmatrix}, \qquad K_{r2}^N = krp \begin{bmatrix} -\sin\varphi_{rp}\sin\alpha_r & -\cos\varphi_{sp}\cos\alpha_s & -\sin\varphi_{sp} \\ -\cos\varphi_{sp}\cos\alpha_s & \cos^2\varphi_{sp} & \cos\varphi_{sp} \\ -\sin\varphi_{sp} & \cos\varphi_{sp} & 1 \end{bmatrix}$$

$$K_{s2}^N = ksp \begin{bmatrix} 0 & 0 & 0 \\ \sin\varphi_{sp}\sin\alpha_s & \sin\varphi_{sp}\cos\alpha_s & -\sin\varphi_{sp} \\ -\cos\varphi_{sp}\sin\alpha_s & -\cos^2\varphi_{sp} & -\cos\varphi_{sp} \\ -\sin\varphi_s & -\cos\varphi_s & 1 \end{bmatrix}$$

The matrices given in Eq. (25) are expressed by:

$$K^N = K_{s3}^p + K_{c3}^p + K_{r3}^p \tag{26}$$

$$K_{c3}^p = \begin{bmatrix} K_p & 0 & 0 \\ 0 & K_p & 0 \\ 0 & 0 & 0 \end{bmatrix}, \qquad K_{s3}^p = kp \begin{bmatrix} \sin^2\alpha_s & \cos\alpha_s\sin\alpha_s & -\sin\alpha_s \\ \cos\alpha_s\sin\alpha_s & \cos^2\alpha_s & -\cos\alpha_s \\ -\sin\alpha_s & -\cos\alpha_s & 1 \end{bmatrix}$$

$$K_{r3}^p = kr \begin{bmatrix} \sin^2\alpha_r & -\cos\alpha_r\sin\alpha_r & -\sin\alpha_r \\ -\cos\alpha_r\sin\alpha_r & \cos^2\alpha_r & \cos\alpha_r \\ -\sin\alpha_r & \cos\alpha_r & 1 \end{bmatrix}$$

The stiffness matrix is expressed as:

$$\mathbf{K}_B = \mathbf{K}_{mB} + \mathbf{K}_{ss} + \mathbf{K}_{bB} \tag{27}$$

## Appendix B. The dynamic condensation

The dynamic behavior of a subsystem $(r)$ is given by

$$[\boldsymbol{H}^{(r)}]\boldsymbol{f}^{(r)} = \boldsymbol{u}^{(r)} \tag{28}$$

where $[\boldsymbol{H}^{(r)}]$ is the $(N \times N)$ inverse of dynamic stiffness, $\boldsymbol{u}^{(r)}$ is the $(N \times N)$ displacement and $\boldsymbol{f}^{(r)}$ is the $(N \times N)$ of applied forces. The degree of freedom can be partitioned into retained (master) DoFs $\hat{\boldsymbol{u}}^{(r)}$ and discarded (slave) DoFs $\check{\boldsymbol{u}}^{(r)}$.

By assuming that no external force is applied at the slave, Eq. (28) can be partitioned in the form:

$$\begin{bmatrix} [\boldsymbol{H}]_{MM} & [\boldsymbol{H}]_{MS} \\ [\boldsymbol{H}]_{SM} & [\boldsymbol{H}]_{SS} \end{bmatrix} \begin{Bmatrix} \left\{\hat{\boldsymbol{f}}^{(r)}\right\} \\ \{0\} \end{Bmatrix} = \begin{Bmatrix} \left\{\hat{\boldsymbol{u}}^{(r)}\right\} \\ \left\{\check{\boldsymbol{u}}^{(r)}\right\} \end{Bmatrix} \tag{29}$$

By eliminating the slave DoFs $\check{\boldsymbol{u}}^{r}$ it is obtained

$$([\boldsymbol{H}]_{MM} - [\boldsymbol{H}]_{MS}[\boldsymbol{H}]_{SS}^{-1}[\boldsymbol{H}]_{SM})\left\{\hat{\boldsymbol{f}}^{(r)}\right\} = \left\{\hat{\boldsymbol{u}}^{(r)}\right\} \tag{30}$$

The condensed receptance matrix $[\boldsymbol{H}]$ can be identified as

$$\left[\hat{H}^{(r)}\right] = [\boldsymbol{H}]_{MM} - [\boldsymbol{H}]_{MS}([\boldsymbol{H}]_{SS}^{-1})[\boldsymbol{H}]_{SM} \tag{31}$$

The submatrices $[\boldsymbol{H}]_{MM}$, $[\boldsymbol{H}]_{Ms}$, $[\boldsymbol{H}]_{SM}$ and $[\boldsymbol{H}]_{SS}$ can be built by using Eq. (17).

## References


[1] R. Parker, J. Lin, Parametric resonance in two stage gears from fluctuating mesh stiffness, Int. J. Gearing Transm. 3 (2001) 127–134.
[2] R. Parker, J. Lin, Mesh stiffness variation instabilities in two stage gear systems, J. Vib. Acoust. 124 (2002) 68–76.
[3] J.D. Smith, F. Cunliffe, D.B. Welbourn, Dynamic tooth loads in epicyclic gears, J. Eng. Ind. 94 (1974) 578–584.
[4] A. Kahraman, R. Singh, Non-linear dynamic analysis of a geared rotor-bearing system with multiple clearances, J. Sound Vib. 144 (1991) 469–506.
[5] A. Kahraman, Effect of axial vibrations on the dynamics of a helical gear pair, Trans. Am. Soc. Mech. Eng. 115 (1993) 33–39.
[6] A. Bodas, A. Kahraman, Influence of carrier and gear manufacturing errors on the static load sharing behavior of planetary gear sets, JSME Int. J. 47 (3) (2004) 908–915.
[7] V. Abousleiman, P. Velex, A hybrid 3D finite element/lumped parameter model for quasi-static and dynamic analyses of planetary/epicyclic gear sets, Mech. Mach. Theory 41 (2006) 725–748.
[8] A. Kahraman, Planetary gear train dynamics, J. Mech. Des. 116 (3) (1994) 713–720.
[9] F. Chaari, R. Hbaeib, T. Fakhfakh, M. Haddar, Dynamic response simulation of planetary gears by the iterative spectral method, Int. J. Simul. Model. 4 (2005) 35–45.
[10] Y. Guo, R.G. Parker, Sensitivity of general compound planetary gear natural frequencies and vibration modes to model parameters, J. Vib. Acoust. 132 (1) (2010).
[11] J. Peeters, D. Vandepitte, P. Sas, S. Lammens, Comparison of analysis techniques for the dynamic behaviour of an integrated drivetrain in a wind turbine, in: Proceedings of ISMA 2002, Department of Mechanical Engineering, K.U. Leuven, Belgium, 2002.
[12] F. Vanhollebeke, J. Helsen, Multibody modelling of varying complexity for modal behaviour analysis of wind turbine gearboxes, Renew. Energy 36 (2011) 3098–3113.
[13] J. Wei, C. Lv, W. Sun, A study on optimum design method of gear transmission system for wind turbine, Int. J. Precis. Eng. Manuf. 14 (5) (2013) 767–778.
[14] J. Wang, D. Qin, T.C. Lim, Flexible multibody dynamic modeling of a horizontal wind turbine drivetrain system, J. Mech. Des. 131 (2009) 1–8.
[15] J. Peeters, D. Vandepitte, P. Sas, Structural analysis of a wind turbine and its drive train using the flexible multibody simulation technique, in: Proceedings of ISMA2006, Department of Mechanical Engineering, K.U. Leuven, Belgium, 2006.
[16] F. Zhipeng, Z.J. Zuo, Vibration signal models for fault diagnosis of planetary gearboxes, J. Sound Vib. 331 (2012) 4919–4939.
[17] B. Jetmundsen, R.L. Bielawa, W.G. Flannelly, Generalized frequency domain substructure synthesis, J. Am. Helicopter Soc. 33 (1) (1988) 55–64.
[18] R.E.D. Bishop, D.C. Johnson, The Mechanics of Vibration, Cambridge University Press, 1960.
[19] D. Otte, J. Leuridan, H. Grangier, R. Aquilina, Prediction of the dynamics of structural assemblies using measured FRF data: some improved data enhancement techniques, in: Proceedings of 9th IMAC, London, 1991, pp. 909–918.
[20] T.C. Lim, G.C. Steyer, An improved numerical procedure for coupling of dynamic components using frequency response functions, in: Proceedings of 9th IMAC, London, 1991, pp. 902–908.
[21] T.C. Lim, J. Zhen, G. Lu, Determination of system vibratory response characteristics applying a spectral-based inverse sub-structuring approach. Part I: analytical formulation, Int. J. Veh. Noise Vib. 1 (2004) 1–30.
[22] B.L. Choi, J.M. Park, Application of the impedance coupling method and the equivalent rotor model in rotordynamics, Finite Elem. Anal. Des. 39 (2) (2002) 93–106.
[23] W. D'Ambrogio, A. Fregolent, Promises and pitfalls of decoupling procedures, in: Proceeding of 26th IMAC, Bethel, CT, USA, 2008.
[24] A. Erturk, H.N. Ozguven, E. Budak, Analytical modeling of spindle-tool dynamics on machine tools using Timoshenko beam model and receptance coupling for the prediction of tool point FRF, Int. J. Mach. Tools Manuf. 46 (2006) 1901–1912.
[25] W. D'Ambrogio, A. Fregolent, The role of interface DoFs in decoupling of substructures based on the dual domain decomposition, Mech. Syst. Signal Process. 24 (2010) 2035–2048.
[26] K. Cuppens, P. Sas, L. Hermans, Evaluation of the FRF based substructuring and modal synthesis technique applied to vehicle FE data, in: Proceedings of ISMA, Leuven, 2003.
[27] W. D'Ambrogio, A. Fregolent, Decoupling procedures in the general framework of frequency based substructuring, in: Proceedings of the IMAC-XXVII, 2009.
[28] A.P. Vale Urgueira, Dynamic Analysis of Coupled Structures Using Experimental Data, PhD thesis, University of London, 1989.
[29] J. Peeters, Simulation of Dynamic Drive Train Loss in a Wind Turbine, PhD thesis, Departement Werktuigkunde, Katholieke Universiteit Leuven, Belgium, 2006.
[30] W. D'Ambrogio, A. Fregolent, Decoupling of a substructure from modal data of the complete structure, in: Proceedings of ISMA2004 International Conference on Noise and Vibration Engineering, Leuven, Belgium, January 2004, pp. 2693–2706.
[31] U. Tabak, B. Besselink, D.J. Rixen, A comparison of model reduction techniques from structural dynamics, numerical mathematics and systems and control, J. Sound Vib. 332 (2013) 4403–4422.
[32] L.E. Suarez, E.E. Matheu, A modal synthesis technique based on the force derivative method, J. Vib. Acoust. 114 (1992) 209–216.

[33] J. Lin, R.G. Parker, Analytical characterization of the unique properties of planetary gear free vibration, J. Vib. Acoust. 121 (1999) 316–321.
[34] P. Sjovall, T. Abrahamssoon, Substructure system identification from coupled system test data, Mech. Syst. Signal Process. 22 (1) (2008) 15–33.
[35] K.M. Al-hussain, I. Remond, Dynamic response of two rotors connected by rigid mechanical coupling with parallel misalignment, J. Sound Vib. 249 (3) (2002) 483–498.
[36] D. de Klerk, D. Rixen, J. de Jong, The frequency based substructuring (FBS) method reformulated according to the dual domain decomposition method, in: Proceedings of the 24th International Modal Analysis Conference, St. Louis, MO, Society for Experimental Mechanics, Bethel, CT, USA, 2006, Paper 136.